IOP Publishing

Metastable argon atom kinetics in a low-pressure capacitively coupled radio frequency discharge

Zoltán Donkó[1,*] ⓘ **, Peter Hartmann**[1] ⓘ **, Ihor Korolov**[2] ⓘ **, David Schulenberg**[2] ⓘ **, Stefan Rohr**[2] **, Shahid Rauf**[3] ⓘ **and Julian Schulze**[2] ⓘ

[1] Institute for Solid State Physics and Optics, Wigner Research Centre for Physics, 1121 Budapest, Konkoly Thege Miklós str. 29-33, Hungary
[2] Chair of Applied Electrodynamics and Plasma Technology, Ruhr-University Bochum, 44780 Bochum, Germany
[3] Applied Materials, Inc., 3333 Scott Blvd., Santa Clara, CA 95054, United States of America

E-mail: donko.zoltan@wigner.hu

CrossMark

Abstract

The kinetics of excited atoms in a low-pressure argon capacitively coupled plasma source are investigated by an extended particle-in-cell/Monte Carlo Collisions simulation code coupled with a diffusion-reaction-radiation code which considers a large number of excited states of Ar atoms. The spatial density distribution of Ar atoms in the $1s_5$ state within the electrode gap and the gas temperature are also determined experimentally using tunable diode laser absorption spectroscopy. Processes involving the excited states, especially the four lower-lying 1s states are found to have significant effects on the ionization balance of the discharge. The level of agreement achieved between the computational and experimental results indicates that the discharge model is reasonably accurate and the computations based on this model allow the identification of the populating and de-populating processes of the excited states.

Keywords: CCP, metastable atoms, TDLAS measurement, PIC/MCC-fluid hybrid simulation

(Some figures may appear in colour only in the online journal)

1. Introduction

Capacitively coupled plasmas (CCPs) are of paramount importance in plasma processing technologies, see, e.g. [1–5]. Modeling and simulation studies have been aiding their applications throughout the years and helped reaching a detailed understanding of the physics of these discharges [6]. The most important methods for the numerical description of CCPs include fluid approaches [7, 8], particle based simulations [9, 10], and the combination of these, termed as hybrid approaches [11, 12]. Particle simulations, which have an advantage that they are applicable in the kinetic domain and eliminate the need for any assumptions about the particle distribution functions, are mostly accomplished using the particle-in-cell method complemented with Monte Carlo treatment of collision processes, see, e.g. [9, 13, 14]. This scheme, known as 'PIC/MCC', has proven to be extremely powerful for the exploration of charged particle dynamics and particle energy distribution functions in a variety of gases and gas mixtures, in CCPs operated under a wide range of conditions (electrode configuration, pressure, driving voltage waveform and amplitude, etc) [15–21].

Most of the PIC/MCC simulations of electropositive discharges in noble gases consider only two charged species: electrons and singly-charged atomic ions of the parent gas

[22]. At higher pressures [23], it is also necessary to consider molecular ions, while in electronegative gases and mixtures, including, e.g. O_2 [24, 25] and CF_4 [26–28], the formation (via electron attachment) and destruction (via recombination or mutual neutralization) of negative ions have to be accounted for as well in the simulations. With the appearance of multiple ionic species, an increasing number of elementary processes needs to be considered [29, 30]. The predictive capability of any discharge model is based on the successful identification of the set of elementary processes that account for the main physical effects in the system and under the specific conditions.

Concerning CCPs operated in noble gases, the effects of metastable atoms on the plasma are usually neglected in PIC/MCC simulations [22, 31], although it has already been recognized and discussed in a number of papers, see e.g. Roberto *et al* [32] and Wen *et al* [33], that besides *electron impact ionization of ground state (GS) atoms* (taking as an example Ar gas),

$$e^- + Ar(GS) \rightarrow Ar^+ + 2e^-, \tag{1}$$
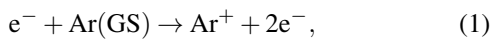
alternative pathways to ionization due to the presence of excited atoms may also become appreciable. These additional ionization processes are *stepwise ionization*:

$$e^- + Ar^* \rightarrow Ar^+ + 2e^- \tag{2}$$

and *pooling ionization*:

$$Ar^* + Ar^* \rightarrow Ar + Ar^+ + e^-, \tag{3}$$
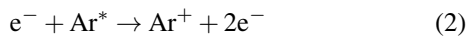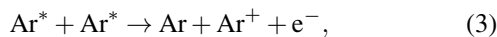
where Ar^* denotes an excited state. Although the densities of the atoms in the excited states are orders of magnitude lower as compared to the density of GS atoms, the lower threshold energies of the stepwise processes may result in significant rates, as the density of low-energy electrons is also orders of magnitude higher compared to the density of those, which are able to excite/ionize atoms from the GS.

The above reactions become prominent in CCPs as demonstrated by Roberto *et al* [32] and Wen *et al* [33] at pressures approaching 1 Torr, when the populations of excited Ar atoms, in particular in the metastable ($1s_5$ and $1s_3$) and the resonance ($1s_4$ and $1s_2$) states acquire significant density and electron impact ionization of GS atoms loses its dominance. Note, that for the designation of the excited states we adopt the *Paschen notation*, because this has been used in most previous papers. A useful 'dictionary' for different notations can be found in the work of Siepa [34].

A behavior similar to that in CCPs was observed in DC discharges as well by Ferreira *et al* [35], where the above processes, via their efficient contributions to ionization, also lower the maintaining electric field of the discharge, in agreement with experiments. This work also pointed out that at low currents and pressures (resulting in a low plasma density) the four Ar 1s (metastable and resonant) states are practically uncoupled, i.e. these are formed by electron impact excitation of GS atoms and are lost by diffusion (metastable states) or by radiation (resonant states). At conditions resulting in higher plasma density, however, a strong coupling between these levels was found to appear; under these conditions the total excited population is efficiently redistributed among these levels. In this process, the higher excited (2p) states play a role, too. The work presented in [36] also showed that the effects of metastable atoms on the discharges can be described accurately only by considering additional higher excited states.

The contribution of the excited states to the ionization in argon CCPs was already addressed in a few previous studies by extending the 'simple' PIC/MCC approach, e.g. in the paper of Lauro-Taroni *et al* [37], while the effects of the presence of Ar atoms in excited states in combination with the effects of an external magnetic field were investigated by Zheng *et al* [38]. In [33, 39], a major advance of the simulations of Ar CCPs was reported by Wen *et al*: the fluid description of Ar atoms in the 1s and 2p states was coupled to the PIC/MCC simulation of the charged species. A significant influence of the presence of these excited states on the plasma density was reported as well as an emerging dominance of the stepwise and pooling ionization processes when the pressure approaches the Torr range. A qualitative agreement between the computed metastable density profiles with experimental data of [40] was claimed to be achieved. Such extensions of models with excited states have been aided by the advance of measurements and calculations of stepwise cross sections [41–46].

The extensions of discharge models with radiative processes leads to the ability to predict the radiation from the plasma as well. Models motivated by this are called *collisional radiative models*, CRM [47–50]. These models are able to predict the distribution of excited states in the plasma as shown by Zhu and Pu [51] as well as spectral line intensities as a function of plasma characteristics (like the electron density and electron temperature) and can thus be used as plasma diagnostics tools [34, 50, 52]. It has been shown by Zhu *et al* [53] that from the optical emission spectrum one can determine the features of the electron energy distribution function and determine the densities of excited atoms in the metastable and resonant states, see, e.g. Boffard *et al* [54] and Kovalev *et al* [55]. The reliability of the determination of the electron temperature and electron density via optical emission spectroscopy and collisional radiative modeling was investigated via a comparison with a Langmuir probe diagnostics for capacitively-coupled and inductively-coupled Ar plasmas by Chai and Kwon [56]. The dynamics of argon metastable and resonance states was also investigated in a pulsed CCP [57].

This technique can be refined by temporal synchronization of the measurements with the plasma driving voltage, resulting in phase resolved optical emission spectroscopy (PROES). Using PROES, the aforementioned quantities can be determined time and space resolved, providing additional insight [58–60].

Besides playing a significant role in stepwise excitation and ionization processes, metastable atoms can as well contribute to the emission of secondary electrons from the electrodes [61] due to their high fluxes toward these surfaces [62]. Their role is expected to vary strongly with discharge conditions [63–65].

It follows from the above thoughts that except for very low pressures, an accurate description of a noble gas plasma requires including a number of excited states in the discharge model. In our work, we follow this route and include 30 excited states of Ar atoms in our model of an Ar CCP. While, as reviewed above, metastable/resonant atoms and atoms in higher excited states have already been included in several modeling studies of radio frequency (RF) discharges, to our best knowledge this is the first work where the *computed spatial density profiles of metastable atoms in a CCP are quantitatively compared with spatially resolved experimental data obtained under identical discharge conditions*. Details of the computational approach are presented in section 2, while the experimental setup and the methods of the measurement of the metastable atom density and the gas temperature are outlined in section 3. The computational results and their comparison with experimental data are presented in section 4 and a summary of our work is given in section 5.

2. Computational methods

The computations are based on two discharge models having different complexity. The first, named here as *'reference model'* is a common type of model that is widely used for low-pressure Ar CCP discharges (e.g. [22]). It includes a set of electron-atom collisions, including elastic scattering, excitation of GS Ar atoms to several higher-energy states, and ionization, as well as elastic ion-atom collisions. This model is implemented into a standard 1D PIC/MCC code.

The extension of the reference model leads to the *'full model'*, which includes several additional types of processes: stepwise excitation, de-excitation, pooling ionization, and radiation processes. Including these processes requires handling a large number of additional reactions due to the numerous (30) excited states considered. The resulting numerical framework consists of two codes: an extended PIC/MCC code and a diffusion-reaction-radiation (DRR) code. The first of these codes handles collisions of the electrons with the Ar atoms in the GS and in the excited states based on the spatial density distributions of the Ar atoms in the excited states taken as input from the previous run of the DRR code. The output of the PIC/MCC simulation includes the rates of all electron impact processes with their spatial distributions. These spatially resolved rates are used as input data in the DRR code to compute the density distributions of the excited states, while also taking into account the radiative processes, quenching reactions of the metastable states, pooling ionization reactions, as well as the diffusion of the excited species. These two codes are executed iteratively to obtain a converged solution for a given set of discharge conditions. This convergence is usually achieved over a few thousands of RF cycles, similarly

to 'standard' PIC/MCC simulations. In the iterative solution of our model, we run the PIC/MCC code for 2–5 RF cycles, then run the DRR module, and then this cycle is repeated. The number of iterations is between hundreds and thousands. The rates of elementary processes are updated after each run of the PIC/MCC code using a moving average. The final results presented in the manuscript were collected during PIC/MCC simulations spanning 200 RF cycles in the converged phase and a subsequent run of the DRR module.

Further details of the codes are given in the following subsections. The gas-phase elementary processes included in the simple 'reference model' and in the 'full model' are listed in table 1.

2.1. The basic PIC/MCC code and its extension

The PIC/MCC code that implements the 'reference model' is based on the basic principles [13, 22] of this simulation technique. The simulation uses the electrostatic approximation and is 1D in real space and 3D in velocity space. The code traces superparticles corresponding to electrons and Ar$^+$ ions (about 10^5 of both types) in a homogeneous background gas having a temperature determined experimentally (see section 3.1). The cross sections of the electron impact processes are taken from the BSR database [66] of LxCat [67, 68], while the formulae given by Phelps [69] are used for the elastic collisions of the ions with Ar atoms: the differential cross section is approximated by an isotropic part and a backscattering part (in the center-of-mass coordinate frame).

The computational grid consists of 600 points and the number of time steps within an RF period ranges between 4000 and 12 000, depending on the pressure. These simulation settings respect the stability criteria of the PIC/MCC scheme [70, 71] for the given discharge parameters. At the electrode surfaces, an ion-induced effective secondary electron yield of $\gamma = 0.07$ and an effective electron reflection coefficient of $r = 0.7$ are adopted [72, 73]. The (time-averaged) Electron Energy Probability Function, EEPF, $f(\varepsilon)$, normalized as $\int f(\varepsilon)\sqrt{\varepsilon}d\varepsilon = 1$ is computed in the PIC/MCC code for the central 10%-wide domain of the discharge. For more details of the basic PIC/MCC approach the reader is referred to, e.g. [22]. We note, that the basic PIC/MCC code has been benchmarked with other independent codes [78] and validated with experiments [72, 73].

In the extended code, besides GS Ar atoms, excited Ar atoms in 30 distinct states as given by Zatsarinny *et al* [79] also appear as targets, with spatially dependent density, for the electron impact collisions. A large number of stepwise excitation processes between these states, for which cross sections are given in [66], are included (see table 1). The model accounts for the 'inverse' of these processes as well, i.e. electron impact de-excitation collisions between the excited states and to the GS. The cross sections of these processes are obtained using the principle of detailed balance, see, e.g. Gangwar *et al* [44].

Stepwise ionization is considered for the four 1s states and the ten 2p states, with cross sections taken from Hyman [74].

Table 1. Gas-phase elementary processes considered in the models. Here, Ar^* and Ar^{**} denote excited states, with $\varepsilon(Ar^*) < \varepsilon(Ar^{**})$. Ar^r and Ar^m represent the lowest resonant ($1s_4$ and $1s_2$) and the metastable ($1s_5$ and $1s_3$) states, respectively. GS stands for the ground state. In the case of processes involving radiation '×2' indicates that both the spontaneous emission and re-absorption processes are included.

Reaction	Name	# of processes	Reference
PROCESSES IN THE REFERENCE MODEL			
$e^- + Ar \rightarrow e^- + Ar$	Elastic scattering	1	[66]
$e^- + Ar \rightarrow e^- + Ar^*$	Excitation of GS atoms	30	[66]
$e^- + Ar \rightarrow 2e^- + Ar^+$	Ionization of GS atoms	1	[66]
$Ar^+ + Ar \rightarrow Ar^+ + Ar$	Elastic scattering (isotropic + backward)	2	[69]
ADDITIONAL PROCESSES IN THE FULL MODEL			
$e^- + Ar^* \rightarrow e^- + Ar$	De-excitation to GS	30	[66]
$e^- + Ar^* \rightarrow e^- + Ar^{**}$	Stepwise excitation	435	[66]
$e^- + Ar^{**} \rightarrow e^- + Ar^*$	De-excitation to excited states	435	[66]
$e^- + Ar^* \rightarrow 2e^- + Ar^+$	Stepwise ionization	14	[74]
$Ar^{r,m} + Ar^{r,m} \rightarrow e^- + Ar^+ + Ar$	Pooling ionization	6	[75]
$Ar^* \leftrightarrow Ar + photon$	Spont. em. and re-abs. to/from GS	7 (×2)	[34]
$Ar^{**} \leftrightarrow Ar^* + photon$	Spont. em. and re-abs. between exc. states	136 (×2)	[34]
$Ar^* \rightarrow wall$	Diffusion to boundaries	30	[56, 76]
$Ar^m \rightarrow Ar$	2- and 3-body quenching by neutrals	2	[77]

(The cross sections from all the 1s states are supposed to be the same, and the same holds for all the 2p levels as well, however, the energy loss in a process depends on the initial excited state.) As an additional source of ionization, the pooling reaction between atoms in any of the 1s states is also considered, with a rate coefficient adopted from Lymberopoulos and Economou [75].

The settings for the gas temperature, the spatial grid, the time step, and the surface coefficients are the same as in the 'reference' simulation. The principal output of the PIC/MCC code is the set of the rates of the electron-impact elementary processes, which determine the spatial density distribution of the excited states. Data for these rates are collected at the points of a grid with 60 points, used in the DRR code, for better signal to noise ratio. Also, these rates are not built based on the number of reactions occurring in the simulations, but by averaging the collision frequencies of the electrons along their trajectories.

2.2. The DRR code

The DRR code computes the densities of the Ar atoms in the various excited states based on the reaction rates obtained in the PIC/MCC simulation and considering, additionally, the diffusive transport of the atoms in the excited states, the rates of the pooling reactions, the quenching of the metastable states by neutral atoms, as well as radiation processes.

The transport of the atoms in the excited states in the direction connecting the electrodes is accounted for by 1D diffusion equations for each of the excited species. The diffusion equations are solved numerically using the forward-time-centered-space method (see Wen *et al* [33]) on a computational grid comprising 60 points. The diffusion coefficient of the metastable atoms is taken to be $D \cdot N = 1.7 \times 10^{20} \, \mathrm{m^{-1} \, s^{-1}}$ (where N is the number density of the background gas atoms)

[76], with a temperature dependence given in [56]. The same coefficient is used for the other excited states as well, however, apart from the metastable and resonant states, no appreciable diffusion exists in the case of the other excited states due to their short lifetimes. The diffusion equations are solved with a boundary condition, which specifies the derivative of the density based on the reflection coefficient (for which a value of $C_{\mathrm{refl}} = 0.5$ is adopted [33]). As an additional loss channel, the radial diffusion losses of the excited species are also included, to better approximate the real geometry of the experimental discharge cell. Pooling ionization reactions of atoms in the 1 s excited states (already mentioned in section 2.1), as well as quenching of the metastable atoms by neutrals described by Tachibana [77] represent additional loss mechanisms.

Among the excited states and between these and the GS we take into account 143 radiative transitions, as listed by Siepa [34] with the corresponding Einstein coefficient values. The inverse of the radiation processes is also considered: the re-absorption of the radiation is accounted for by adopting an escape factor based on [80, 81]. (More precisely, we use equations (6a) and (6b) of [81], which originate from [80], but in [81] typographical errors of the corresponding equations of [80] have been corrected.)

2.3. Coupling of the codes

The PIC/MCC and the DRR codes are executed iteratively until a converged solution is found for the set of discharge conditions. Typically, after simulating a few RF cycles by the PIC/MCC code, the DRR code is run for a time span of 10^{-6} s. Convergence of the excited state densities and profiles is achieved over several thousands of RF cycles as in a conventional PIC/MCC simulation. Due to the high number of target species (with spatially varying

densities) and associated reaction channels, the simulations are rather time-consuming. Reaching convergence requires weeks-months of run time with an Intel Xeon Gold 5320 H CPU. The dominant part of this run time is consumed by the PIC/MCC simulation.

3. Experiment

The experiments are motivated by the determination of the spatial distribution of the Ar $1s_5$ metastable atoms in the discharge as well as the gas temperature. These measurements are accomplished by tunable diode laser absorption spectroscopy (TDLAS), with a setup sketched in figure 1.

The measurements are performed in a plasma reactor, which consists of two plane parallel stainless steel electrodes with a diameter of 119 mm placed inside a borosilicate glass cylinder with an inner diameter of 120 mm. The gap between the electrodes is set to 30 mm. Before the measurements, the system is pumped down to a base pressure below 10^{-4} Pa. The discharge is operated in Ar gas of 6.0 purity. The flow rate is kept in the domain of 1–3 sccm and the pressure range for the measurements is 2.5–150 Pa. A detailed description of the reactor and the gas handling system can be found elsewhere [72]. The reactor is operated with a driving frequency of 13.56 MHz by means of an RF generator (Advance Energy Cesar 136) and an impedance matchbox (Advance Energy VarioMatch 1000). The voltage at the powered electrode is monitored with a high-voltage probe (PMK PHVS 662-L-RO) connected to an oscilloscope (LeCroy LT364).

3.1. TDLAS setup

The $1s_5$ argon metastable density and the gas temperature in the plasma are measured by TDLAS [82–86]. The density and the temperature of the Ar $1s_5$ atoms are obtained from the measured absorption profile of the Ar $1s_5 \rightarrow$ Ar $2p_6$ transition at $\lambda = 772.376$ nm. The density is obtained from the depletion of the light intensity, while temperature (which is assumed to be equal to the argon gas temperature) is determined from the width of the profile. To accomplish these measurements, we employ two detection techniques: (i) 'photodiode measurement', in which we use a photodiode to measure the light intensity of a laser beam passing through the center of the plasma, as well as (ii) 'camera measurement', for which we use an intensified charge-coupled device (ICCD) camera to record the intensity of this beam spatially resolved along the electrode gap.

The laser head is equipped with a fiber coupler to guide the laser beam via single-mode optical fibers. The line width of the laser is below 1 MHz which is significantly smaller than the Doppler width of the absorption line profile ($\approx$800–900 MHz). The head is attached to a diode laser controller (DLC, Toptica Photonics AG) connected to a computer. The laser system is operated in the current controlled mode and allows linear mode-hop-free tuning over the absorption line. The repetition

rate of the frequency sweep is set to 5 Hz. In the first step, the laser beam is split via a single-mode fiber splitter (Thorlabs TN785R2A1). The first part of the beam corresponding to $\approx$90% of the initial intensity is guided into a Fabry–Perot interferometer (FPI) with a built-in photodetector (Toptica FPI 100-0750-3V0 with 1 GHz free spectral range and resolution of $\approx$2 MHz) to detect any unexpected mode hopping and to measure the relative frequency change of the laser light. The second part of the laser beam is split further into two parts. (i) Approximately 10% of the light is guided through the middle of the reactor ($x = 1.5$ cm) to a biased photodiode (Thorlabs DET10N2 with an active area diameter of 1 mm) using a single-mode Pigtailed GRIN fiber collimator (Thorlabs 50-780-APC). The laser power measured at the photodetector is approximately 10 μW mm^{-2} which is low enough to avoid any saturation effects. The signals from this photodiode (used for the measurements in the center of the plasma) and the FPI are recorded by an oscilloscope (PicoScope 6402 C) synchronized with the laser scanning frequency. The data are recorded with a resolution of 4064 points per GHz of laser light frequency change. (ii) The remaining part of the light is guided through another single-mode collimator (Thorlabs F280APC-780) generating a beam with a waist diameter of $\approx$4 mm. This beam is then expanded in one direction with a cylindrical lens (L1) and then collimated using another cylindrical lens L2, to have dimensions along the major and minor axes of, respectively, 65 mm and 4 mm, leading to a power density of $\approx$0.6 μW mm^{-2}. The major axis coalesces with the x direction that is perpendicular to the electrodes (with $x = 0$ corresponding to the position of the grounded electrode) and the minor axis y is parallel with the electrodes (perpendicular to the x axis). This beam is then guided in a way that its elliptical center passes through the geometric center of the glass cylinder.

In order to detect the laser light parallel to the electrode gap and to reduce the consequences of interference effects leading to speckle patterns in the coherent imaging system, a telecentric lens (Thorlabs MVTC23013 0.128$\times$) together with a gated ICCD camera (Stanford Computer Optics 4Picos) is used. To reduce noise, the lens is equipped with a bandpass filter (Thorlabs FL770-10, 770 nm, and full width at half maximum (FWHM) = 10 nm). The camera and the lens provide a spatial resolution of 146 μm per pixel, i.e. 205 pixels over the 3 cm electrode gap. The spatial resolution of the measured metastable atom density is defined not only by the pixel size but also by the imperfection of the optical system including the glass cylinder, and it is estimated to be better than 0.5 mm. Each frame of the camera measurements is synchronized with the laser sweep frequency. The gate width (typically below 50 μs) and the integration time are set in a way to cover 70%–80% of the dynamic intensity range of the camera. This gate width corresponds to about 1 MHz change of the laser frequency. The time between the camera measurements and the trigger signal is controlled by employing the internal delay circuit of the camera. The data are recorded with a resolution of $\approx$30 frames per 1 GHz.
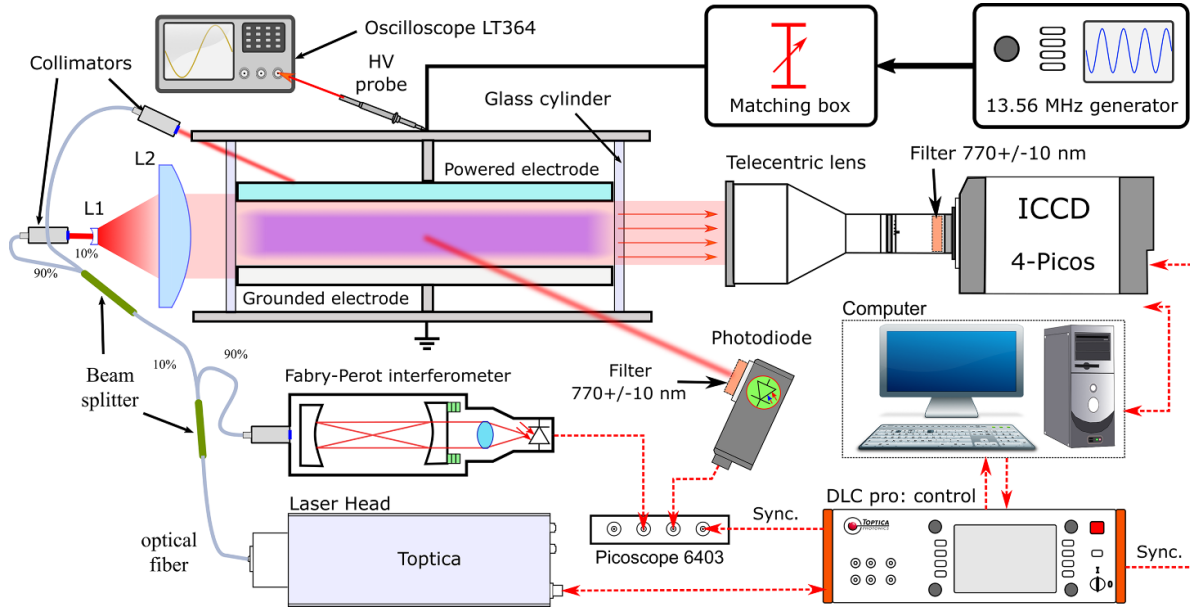
Figure 1. Scheme of the TDLAS experimental setup for the argon metastable atom density and gas temperature measurements.

### 3.2. Data evaluation procedure: argon metastable density and gas temperature measurements

The Beer–Lambert law is applied to obtain absolute metastable atom densities from the measured transmittance:

$$T_{\nu,x} = \frac{I(\nu,x)}{I_0(\nu,x)} = \frac{I_{\text{Pon}}^{\text{Lon}}(\nu,x) - I_{\text{Pon}}^{\text{Loff}}(\nu,x)}{I_{\text{Poff}}^{\text{Lon}}(\nu,x) - I_{\text{Poff}}^{\text{Loff}}(\nu,x)} = e^{-k(\nu,x)l}, \quad (4)$$

where $I(\nu,x)$ and $I_0(\nu,x)$ are the intensities of the transmitted radiation as a function of the laser frequency ν and position x with and without the plasma, respectively. The absorption length, l, is assumed to be equal to the inner diameter of the glass cylinder of 120 mm. In order to take into account the noise of the electronics and the light emission from the plasma, four measurements in total are performed: the intensity of the transmitted radiation with (1) plasma and laser switched on, $I_{\text{Pon}}^{\text{Lon}}(\nu,x)$, (2) plasma on and laser off, $I_{\text{Pon}}^{\text{Loff}}(\nu,x)$, (3) plasma off and laser on, $I_{\text{Poff}}^{\text{Lon}}(\nu,x)$, and (4) plasma off and laser off, $I_{\text{Poff}}^{\text{Loff}}(\nu,x)$.

For the measurements with the camera, these signals are recorded by averaging 5–10 frames for each value of the laser frequency. Each frame image for a specific ν is then cropped to the area where the laser light intensity is above $\sim$70% of its maximum value (resulting in an area of $x \times y = 30 \times 3 \text{ mm}^2$) and then averaged along the y direction to obtain $I(\nu,x)$. An example of the spatially and frequency-resolved absorption signal $k(\nu,x)l$ obtained from the 'camera measurements' is shown in figure 2.

At the time of 'camera measurements', the reference signal from the photodiode is also recorded at the position $x = 1.5$ cm. Each $I(\nu,x)$ photodiode signal (see equation (4)) is averaged for 100–500 scans. This 'photodiode measurement' has a much better signal-to-noise ratio and a higher frequency resolution, but at the same time to perform scanning measurements
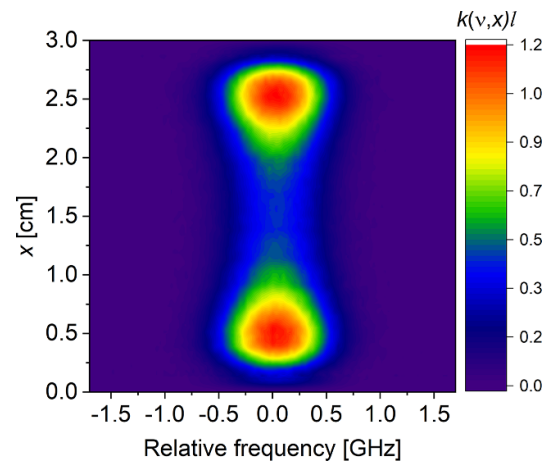

Figure 2. An example of the spatially and frequency-resolved absorption signal obtained from the 'camera measurements'. Discharge conditions: $V_0 = 150$ V RF voltage amplitude and $p = 50$ Pa pressure.

over the electrode gap with this approach would technically be much more challenging and time-consuming, as compared to the 'camera measurement'. An exemplary absorption signal in the plasma obtained from the photodiode and the camera measurements at $x = 1.5$ cm together with the Fabry–Perot signal are shown in figures 3(a) and (b).

Knowing the absorption coefficient $k(\nu,x)$, the density of the Ar $1s_5$ metastables, n_{m}, can be determined from [87]:

$$k(\nu,x) = \frac{e^2}{4\varepsilon_0 cm_e} fn_m F(\nu,x), \quad (5)$$

where e is the elementary charge, ε_0 is the vacuum permittivity, c is the speed of light in vacuum, m_e is the electron mass,
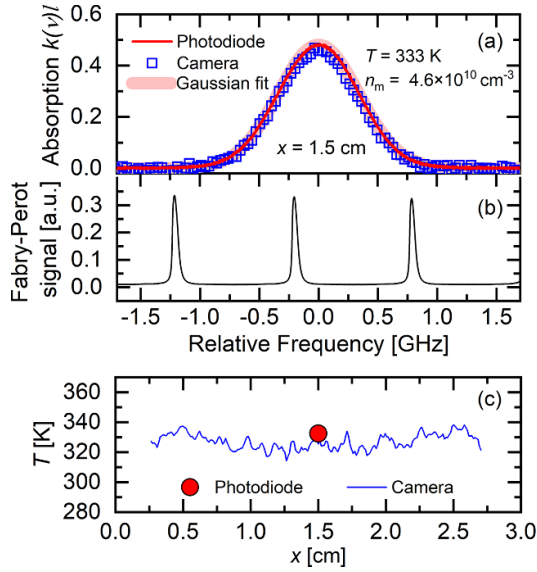
Figure 3. (a) Exemplary absorption signal obtained from the photodiode and the camera measurements in the middle of the electrode gap, $x = 1.5$ cm. Gaussian fit is applied to the photodiode signal. (b) Signal obtained from the Fabry–Perot interferometer. (c) Temperature profile obtained from the absorption signal (see figure 2) and the value calculated from the photodiode signal at $x = 1.5$ cm. Discharge conditions: $V_0 = 150$ V, $p = 50$ Pa.

$f = 0.0278$ [88] is the oscillator strength. $F(\nu,x)$ is a normalized function ($\int_0^{+\infty} F(\nu,x)\mathrm{d}\nu = 1$), which represents the absorption line shape. Based on equations (4) and (5) the absolute line-averaged density, n_m, can be determined using the area, S, under the line-absorption curve:

$$\int_0^{+\infty} \ln(T_{\nu,x}^{-1})\mathrm{d}\nu = S = \frac{e^2 f l}{4\varepsilon_0 c m_\mathrm{e}} n_m. \qquad (6)$$

The metastable densities determined from the camera and the photodiode measurements do not differ more than 5% for all conditions used in this paper. The estimated uncertainty of the absolute metastable density is up to 20%. It is mainly caused by the assumption that the absorption length is equal to the electrode diameter and the metastable density is uniformly distributed in the radial direction. In reality, a radial density profile, depending as well on the axial position, definitely exists in the system, but can only be investigated in more complex measurements in conjunction with 2D PIC/MCC simulations.

At the pressures used in this work, the shape of the absorption line can be described by the Gaussian function due to the Doppler-broadening being dominant. (During the fitting procedure of the measured absorption line profiles, we have not observed any noticeable deviation from the Gaussian shape caused by, e.g. collisional broadening.) In this case, the width (FWHM) of the function is related to the temperature T of the absorbing metastable species, which is assumed to be equal to the gas temperature:
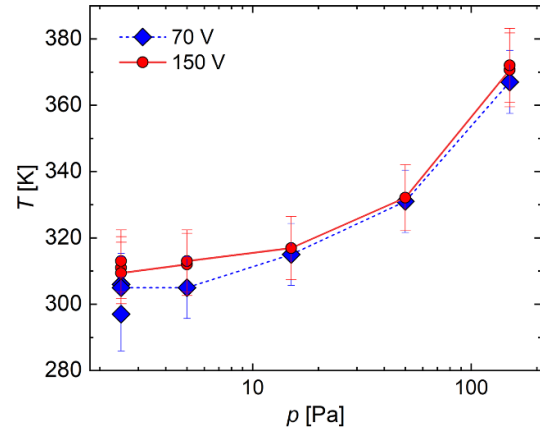
Figure 4. Gas temperature as obtained from the TDLAS measurements as a function of the gas pressure for RF voltage amplitudes of 70 V and 150 V. The multiple data points at the lowest pressure correspond to repeated measurements. The error bars represent uncertainties of the measured data points.

$$\Delta\nu_\mathrm{D} = \lambda^{-1}\sqrt{8\ln(2)k_\mathrm{B}T/M_\mathrm{Ar}}, \qquad (7)$$

where k_B is the Boltzmann constant, and M_Ar is the mass of argon atoms. The uncertainty of the gas temperature is estimated to be below 3% and is mainly due to the accuracy of the Fabry–Perot measurements and the stability of the laser system. The example of the temperature profile obtained from the absorption profiles is shown in figure 3(b). The data for $x < 0.25$ cm and for $x > 2.75$ cm are cut since the signal-to-noise ratio and the quality of the Gaussian fit are significantly reduced in these regions due to the very low absorbance signal. We find that, within the accuracy of the measurements, the temperature can be assumed to be constant along the gap for fixed discharge conditions, which is consistent with the findings of Derzsi *et al* [89], where the spatial distribution of the temperature profile was computed based on a heat conduction model.

Figure 4 shows the measured gas temperature as a function of the gas pressure. Similar to the findings of Schulenberg *et al* [72], the gas temperature is found to be weakly dependent on the applied voltage amplitude but strongly increases with the gas pressure. At low pressure, the gas temperature is close to room temperature, and reaches values of ≈ 370 K at the highest pressure of 150 Pa.

Taking into account the observation that the temperature can be considered to be constant over the whole electrode gap, the signal-to-noise ratio of the measured metastable atom density profiles can be significantly improved by longer measurements of $k(\nu,x)$ with the camera at the frequency ν_max, where the absorbance has its maximum. This way the time of the measurement is shorter as there is no need to scan over the line profile. Consequently, there is less influence of the limited stability of the discharge and the laser system. The metastable density can be calculated from $k(\nu_\mathrm{max},x)$ using the temperature, T, obtained from the 'photodiode measurement'. The data measured using this method are shown in the

figures in the next section. The day-to-day reproducibility of the obtained values is within 5%–10% for the metastable density for the temperature, confirming the stability of the system. The data evaluation and fitting procedures are performed automatically after the absorption signal is measured by using a LabView code.

4. Results

Here, we present the results of the discharge simulations obtained with the 'reference' and 'full' discharge models and provide a comparison between the computed and the measured spatial density distributions of the 1s$_5$ state. Subsequently, the dynamics of the processes populating and de-populating this state are discussed. The discharge conditions correspond to the experimental studies; the CCP is driven by an RF voltage with an amplitude of $V_0 = 70$ V or 150 V, at a frequency of $f = 13.56$ MHz, and the Ar pressure ranges from $p = 2.5$ Pa to 150 Pa. The electrode gap is $L = 3$ cm. The calculations are carried out with the measured gas temperature values, shown in figure 4.

4.1. The effect of excited states on the plasma characteristics

First, we address the effects of the presence of atoms in excited states and the elementary processes associated with these states, on the basic plasma characteristics: the electron density, the EEPF, and the ionization rate.

Figure 5(a) shows the pressure dependence of the peak electron density (that always occurs at the center of the plasma) as obtained from the 'reference' and the 'full' PIC/MCC simulations, while panel (b) of the same figure presents the spatial distribution of the electron density for selected conditions. Figure 5(a) reveals that at the lowest pressures (2–5 Pa) the excited states do not affect the electron density. This, however, does not remain the case as the pressure increases. The trends are the same at both excitation voltage amplitudes of 70 V and 150 V. At 150 Pa, the full simulation in both of these cases predicts a remarkable, about a factor of four higher density as compared to the reference simulation. The cases analyzed in figure 5(b) confirm that the spatial distribution of n_e is unaffected at low p by the excited states in the simulation, whereas at high p a significant increase in the magnitude of n_e is seen, as well as a change of the spatial profile, $n_e(x)$. In the absence of excited states in the model, we obtain a flat $n_e(x)$ profile in the bulk plasma, which can be explained by the fact that ionization of the Ar atoms by electron impact is concentrated to regions of the sheath edges (see later and also in [31]). The profile that is obtained with the full model peaks at the center, indicating the presence of ionization processes in the central region of the plasma as well.

The differences discussed above originate primarily from the increasing importance of stepwise (2) and pooling (3) ionization processes, which is clearly confirmed by figure 6 that shows these contributions as well as the contribution of electron impact ionization of GS Ar atoms, to the total ionization rate. At the low pressure of 5 Pa (see panels (a) and (b) for 70 V and 150 V RF voltage amplitudes, respectively), ionization is dominated by collisions of electrons with GS Ar atoms, the stepwise and pooling processes have about two orders of magnitude lower rates throughout the electrode gap. This situation changes completely at higher pressures. Taking the 150 Pa case as an example (see figures 6(c) and (d)) the ionization of GS atoms has a high rate near the electrodes (actually near the positions corresponding to the maximum width of the sheaths) only, but as the electrons deposit their energy acquired near the edge of the expanding sheath [90] within a short distance due to their short inelastic free path, this rate decreases rapidly. Ionization within the central domain of the plasma is dominated by stepwise ionization, but pooling ionization, has a significant share as well in the ion production. These results show a completely different picture of the discharge maintenance at this high pressure (150 Pa) when excited states are taken into account in the simulations, similarly to that found in [33].

Figure 7 compares the EEPFs obtained from the reference vs. the full simulations, for various discharge conditions. At the low pressure of 5 Pa (panel (a)), no observable changes of the EEPF occur when the reference model is replaced by the full model. At 15 Pa (panel (b)), the distribution functions get slightly depleted in the range of electron energies above a few electron Volts. This trend, caused by the low-energy-threshold stepwise excitation and ionization processes, becomes more pronounced as the pressure is further increased to 50 Pa and 150 Pa, as shown in figures 7(c) and (d), respectively. At the highest pressure, e.g. a factor of 20 to 30 depletion of the electron population is found near the excitation threshold of GS atoms (≈ 11.5 eV).

4.2. Density distributions and kinetics of excited states

In figure 8, we present the spatial distribution of the densities of Ar atoms in the 30 excited states considered in the model, for $V_0 = 150$ V RF voltage amplitude and $p = 5$ Pa (left column) and 150 Pa (right column). The density distributions for the 14 lowest lying excited states (four 1 s states and ten 2p states) are shown in panels (a) and (b), while the densities of Ar atoms in the higher excited states are displayed in panels (c) and (d). At 5 Pa argon pressure, the density of each of the species peaks at the centre of the electrode gap. The 1s$_5$ state exhibits the highest density, at a value of $\approx 2 \times 10^{10}$ cm^{-3}. The density of the other metastable state (1s$_3$) is about an order of magnitude lower, while the 1s$_4$ and 1s$_2$ resonant states are present with a density that is lower by an additional order of magnitude. The density of the 2p states is rather low, ranging between $\approx 5 \times 10^4$ cm^{-3} and $\approx 8 \times 10^5$ cm^{-3}. The densities of Ar atoms in the higher excited states (see figure 8(c)) span a range that is about an order of magnitude lower as compared to the range of densities of Ar atoms in the 2p states. The ratios of the densities of Ar atoms in the metastable and resonant states as well as in 2p states are similar to those reported by Wen *et al* [33] for a low-pressure case of 0.05 Torr.
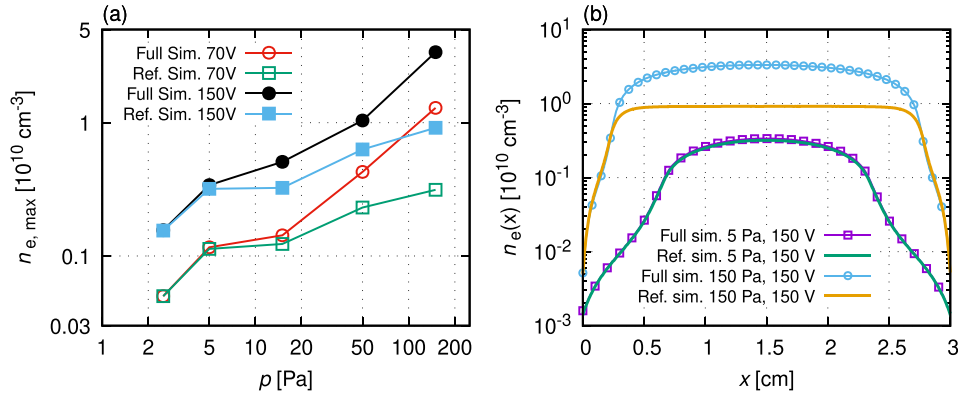
Figure 5. Effects of the Ar* excited states on the plasma characteristics: dependence of the maximum electron density on the gas pressure at $V_0 = 70$ V and 150 V (a) and spatial distribution of the electron density for selected conditions (b). 'Full Sim' and 'reference Sim' correspond to the two discharge models with different complexities.
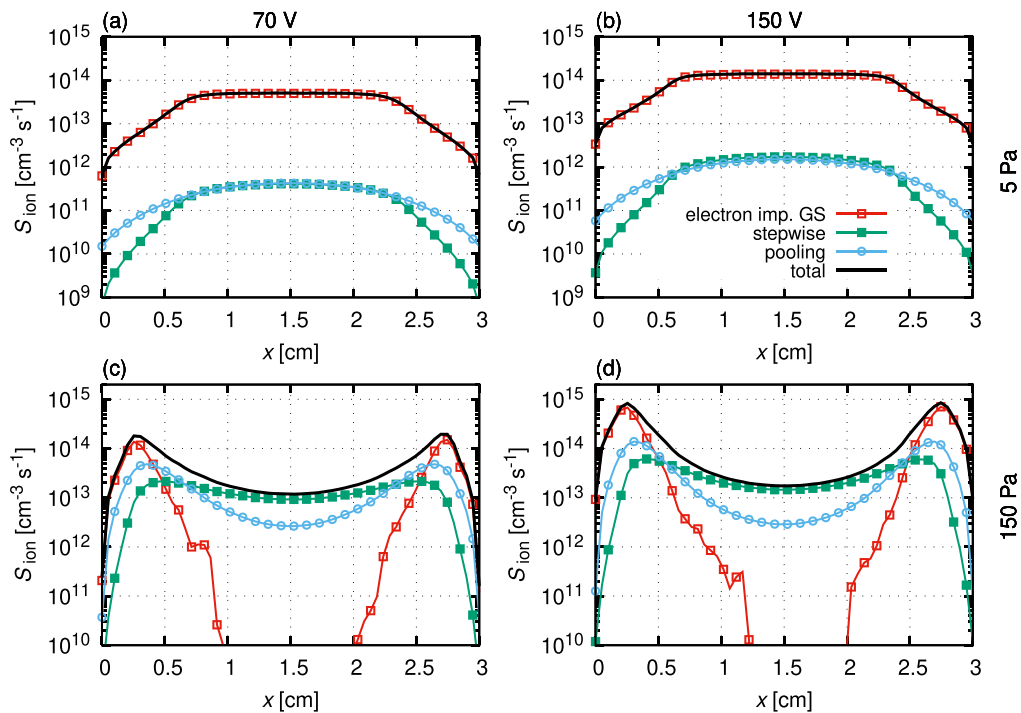

Figure 6. Spatial distributions of the total ionization rate as obtained from the full PIC/MCC simulations, as well as the contributions of electron impact ionization from the ground state (GS), stepwise ionization, and pooling ionization, at $p = 5$ Pa (a), (b) and 150 Pa (c), (d), at 70 V and 150 V RF voltage amplitudes.

When the pressure is increased to 150 Pa, the density distributions undergo a characteristic change: similarly to the electron-impact ionization rate (figure 6) they develop peaks near the electrodes, which shows the importance of the electron-impact excitation of GS Ar atoms in establishing these excited atom populations. On the other hand, the distributions have only a relatively shallow dip around the centre of the discharge, indicating the importance of the effects of the stepwise excitation and de-excitation processes. The density of the Ar $1s_5$ atoms in the centre of the plasma is only moderately higher at 150 Pa as compared to that at 5 Pa. The density of the other 1s states (especially the resonant states), on the other hand, increases significantly with the increasing pressure. This is also true for the lower-energy $2p$ states (especially for $2p_{10,9}$), while the densities of some higher-energy states, like $2p_1$, which is known to be created preferentially by electron impact from the GS, remain relatively low, at a level of $\approx 10^5$ cm^{-3}. The density of atoms in the higher excited states, shown in figure 8(d), is increased as compared to the low-pressure case as well, their spatial profiles also exhibit two peaks near the RF sheath boundaries.

In figure 9, we compare the computed and measured spatial distribution of the density, n_m, of the $1s_5$ state for various pressures and at RF voltage amplitudes of 70 V (panels (a,c)) and 150 V (panels (b,d)). Panels (a) and (b) show the computational, while panels (c) and (d) present the measured
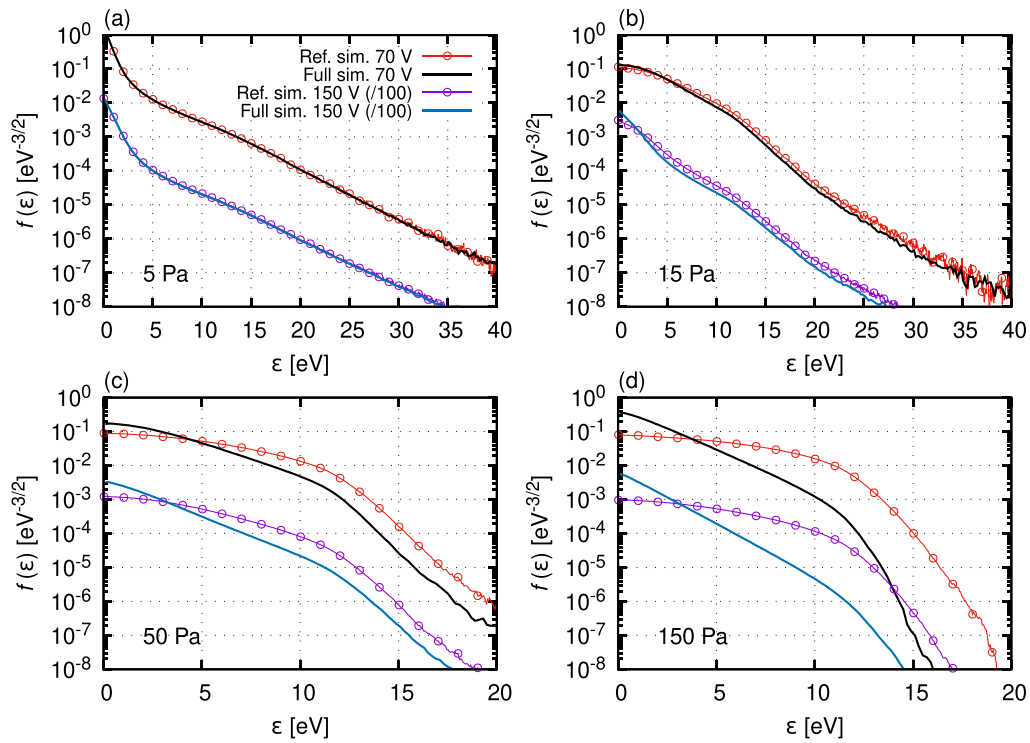
Figure 7. Comparison of the EEPFs obtained from the PIC/MCC simulations based on the 'reference' (thin lines with symbols) and 'full' (thick lines) models, for various pressures and discharge voltages. Note, that the curves corresponding to the higher discharge voltage are shifted vertically by a factor of 100 for a better visibility (see '/100' in the legends).

data. The overall qualitative agreement between these two data sets is very good. At low pressures, the density of the metastable atoms peaks in the center of the discharge and decays towards the electrodes. This behaviour is explained by the production of these species in the central region of the plasma and their diffusive transport toward the electrodes.

With increasing pressure, the density distribution first develops a more flat profile in the central region of the plasma and, subsequently, two peaks, which approach the electrodes. These distributions, while many processes contribute to the balance of the densities, are largely determined by the source functions by electron impact excitation of this state from the GS (see later). It is a consequence of this that n_m at the center of the plasma first increases with increasing pressure, but at higher pressures this trend reverses.

At the lower pressures there is a good agreement between the computational and the experimental results. With increasing pressure ($p > 5$ Pa), however, the computations yield systematically higher densities for the metastable atoms, up to about a factor of two, as compared to the measured values. To understand the deviations that we observe here we have to emphasize that the simulations are spatially one dimensional, while the measurements yield the *line average* of the *radially varying metastable atom density* in the plasma source that has a cylindrical symmetry. In this CCP source, a radial profile of the metastable density clearly exists and this is missed by the simulations, although a radial loss term for the excited species is included in the respective diffusion equations. As the density of the metastable atoms can be supposed to decay significantly

towards the radially limiting surface of the cell, the simulations are expected to overestimate the metastable density.

Besides the above effect, which we believe to be the dominant one responsible for the deviations observed here, deviations can also originate from the limited accuracy of the rather extensive set of input data of the model. We note, e.g. that an earlier investigation of the electron-impact transition between the $1s_5$ and $1s_4$ states of Ar by a laser pump–probe technique by Carbone *et al* [91] concluded that the quantum mechanical calculations presented by Zatsarinny *et al* [79] underestimate the cross sections for electron impact transfers between the Ar 1s states. As among the states the $1s_5$ appears to have the highest density, a stronger coupling could decrease this, bringing the computed data nearer to the measured ones. Another possible cause of the differences, and for the overall accuracy of our model can be the consideration of a limited set of excited states. The simulations indicate that there is a significant electron impact excitation of GS Ar atoms to higher-energy states, which are not included in the calculations of excited state densities. Electron-impact de-excitation of these states as well as radiative transitions originating from these states can clearly influence the populations of the low-lying excited states to some extent as shown by Bogaerts *et al* [47].

Density profiles for metastable atoms similar to those shown in figure 9 were also found by Lymberopoulos and Economou [75] who investigated a plasma source with plane-parallel electrodes using a one-dimensional fluid simulation based on a coupled glow-discharge/neutral-transport-reaction model. Their model included relatively few states and
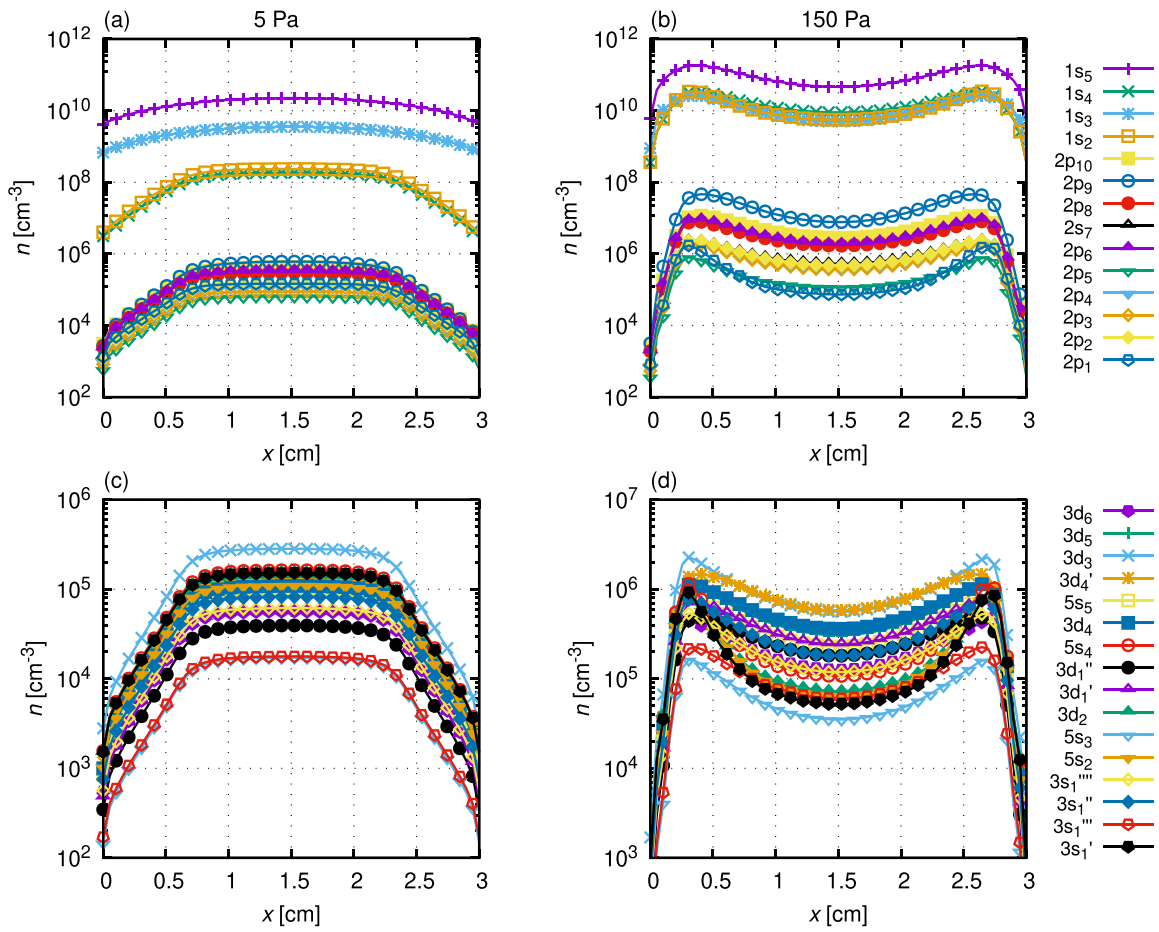
Figure 8. Spatial density distributions of Ar atoms in the 1s and 2p excited states (a), (b) and in higher excited states (c), (d), for $V_0 = 150$ V RF voltage amplitude and $p = 5$ Pa (left column) and 150 Pa (right column). The excited states are identified using the Paschen notation [34].
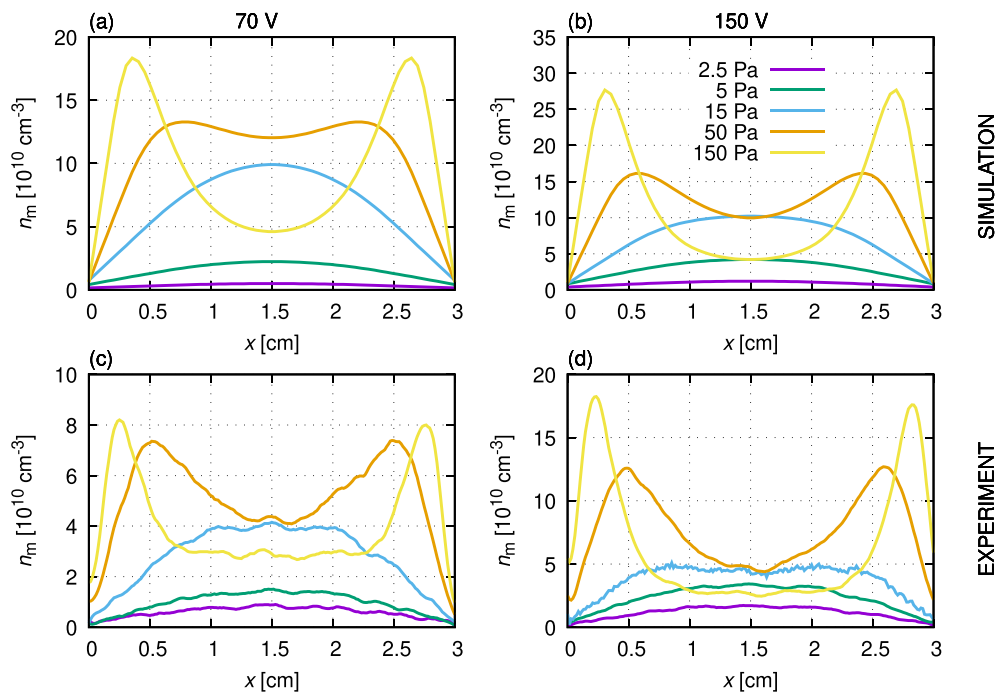
Figure 9. Comparison of the measured and calculated density (n_m) profiles of the Ar 1s$_5$ metastable atoms, for a set of gas pressures and RF driving voltage amplitudes.
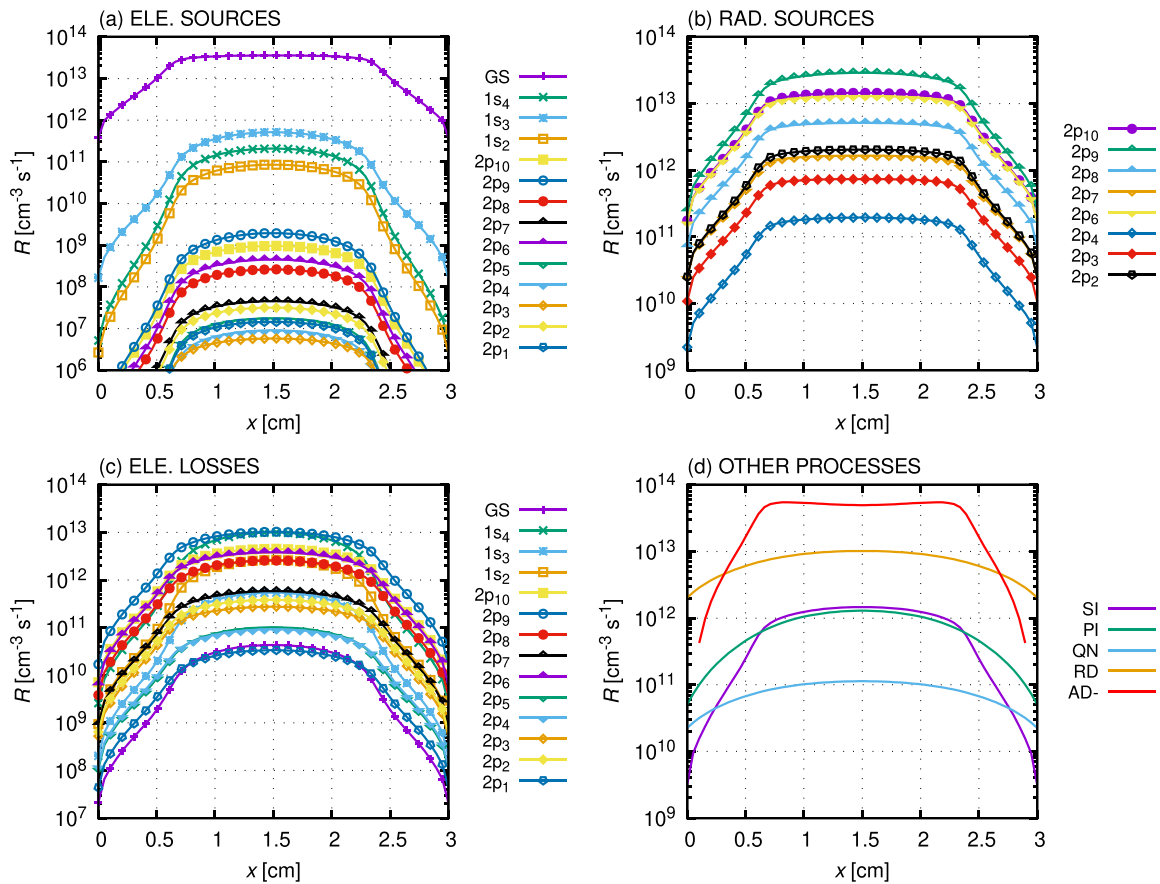
Figure 10. Rates of elementary processes that populate/de-populate the Ar $1s_5$ state at $p = 5$ Pa and $V_0 = 150$ V: (a) populating processes by electron impact excitation from the ground state ('GS') and by de-excitation from higher excited states, (b) populating processes via radiative transitions from 2p states, (c) de-populating processes by stepwise electron impact excitation to higher energy states, and (d) additional processes: 'SI', 'PI', 'QN', 'RD', and 'AD$-$' denote, respectively, stepwise ionization, pooling ionization, quenching by neutrals, radial diffusion loss, and axial diffusion loss. The radiative populating rates already consider the partial trapping of the radiation by using an escape factor (see section 2.1).

reactions, but captured well the main physical processes in the RF discharge operated at 13.56 MHz frequency, 2.54 cm electrode gap, 1 Torr pressure, and 50–100 V voltage amplitudes. Due to the relatively high pressure, the density of the metastable atoms exhibited a profile with two peaks, close to the electrodes, similarly to the findings of our work shown in figure 9. The peak density values found in [75] were in the range of $\approx 3 - 6 \times 10^{11}$ cm^{-3}, approximately a factor of two higher as compared to the present data obtained at comparable RF voltage amplitudes. While metastable densities in this range seem to be typical in CCPs operated at low pressure ($\lesssim 1$ Torr), orders of magnitude higher densities can be achieved in discharges operated at atmospheric pressure, as done, e.g. in the work reported by Yamasaki *et al* [92]. In this work, the plasma was ignited in a microcell with characteristic dimensions of ≈ 1 mm, with a 13.56 MHz RF voltage with 500 V amplitude. Argon metastable atom densities in excess of 10^{14} cm^{-3} were computed in the vicinity of the powered electrode. The calculations that included the heating of the gas and the formation of molecular argon ions confirmed the importance of the stepwise ionization process in the sustainment of the discharge.

Next, we provide additional insight into the population/de-population balance of the Ar $1s_5$ atoms. Figure 10 shows the sources and losses of these excited atoms for $p = 5$ Pa pressure and $V_0 = 150$ V RF voltage amplitude. Panel (a) shows the sources by electron-impact excitation from the GS and electron impact de-excitation from higher 1s and 2p excited states. At this low pressure, the electron impact excitation of GS Ar atoms clearly dominates $1s_5$ production among the electron-impact sources. The source of this state by electron impact from other 1s states is about two orders of magnitude lower and the 2p states provide an even much lower source for populating the $1s_5$ metastable state. The radiative transitions (see figure 10(b)), especially from the $2p_9$, $2p_{10}$, and $2p_6$ states populate this state appreciably, with a rate that is comparable to the electron-impact excitation of GS atoms. The loss rates of the $1s_5$ atoms due to different processes are shown in figures 10(c) and (d). The main electron-impact loss channel appears to be stepwise electron impact excitation to the $2p_9$ state (and to a few other 1s and 2p states with somewhat lower rates). Diffusion losses toward the electrodes as well as the radial diffusion to the chamber wall (see curves 'AD$-$' and 'RD' in figure 10(d)) are the most prominent losses.
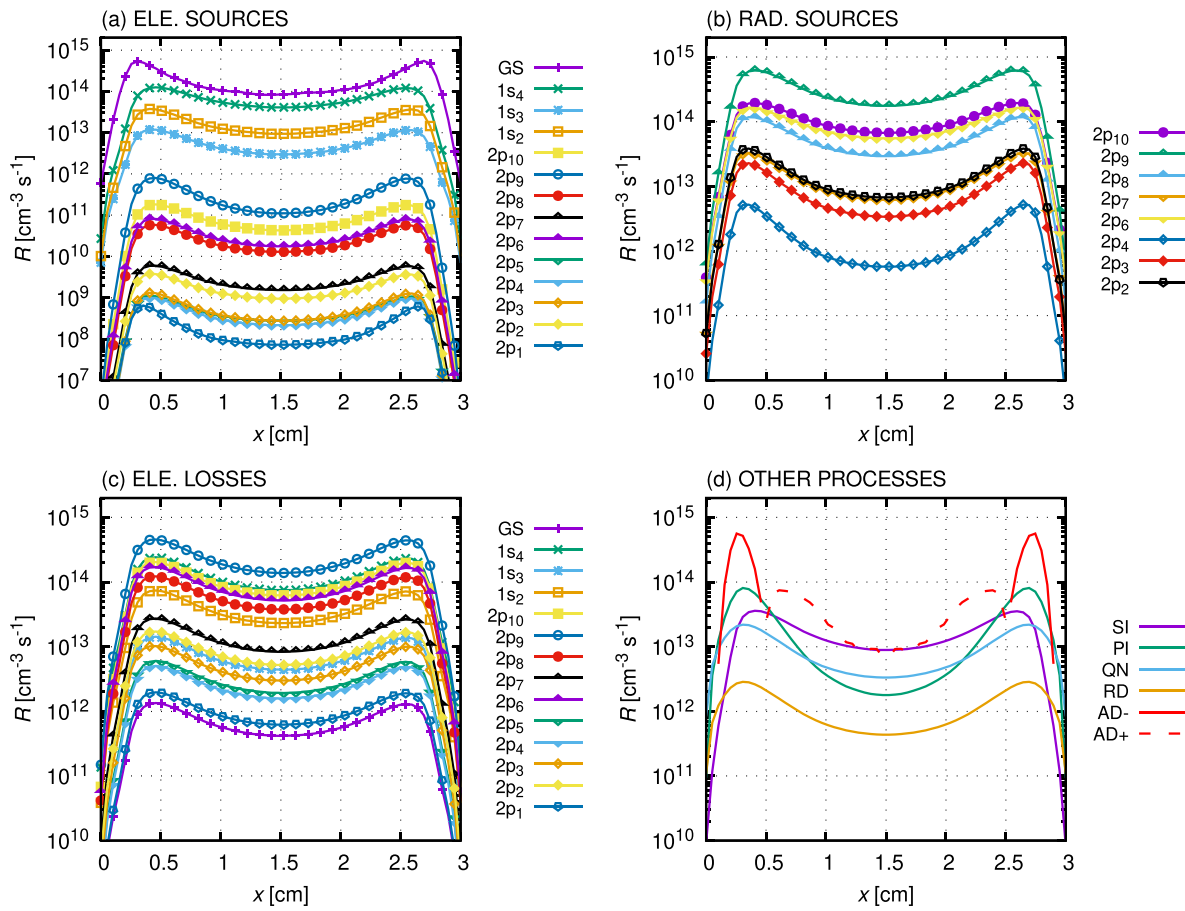
Figure 11. Same as figure 10, but for $p = 150$ Pa. In addition to the processes listed there, in this case diffusion in the axial direction can also give rise to a source of the 1 s$_5$ atoms in the central region of the discharge, the corresponding curve is denoted by 'AD+'.

With the increase of the pressure, the spatial distribution of the rates of the different processes acquires a characteristic shape; both the sources and losses of Ar 1s$_5$ atoms exhibit two peaks close to the electrodes and a dip in the center of the electrode gap, as it can be seen in figure 11. Compared to the low-pressure case discussed above, de-excitation from the other 1 s states contributes more significantly to the production of Ar 1s$_5$ atoms by electron-impact processes. The creation of these metastable atoms is dominated by electron impact excitation of GS Ar atoms and by radiation from the 2p$_9$ state (see panels (a) and (b) of figure 11). The main loss channels are the stepwise electron impact excitation collisions to other excited states, especially to the 2p$_9$ state, as shown in panel (c). Among the additional reactions considered the pooling ionization process has an appreciable rate, however near the electrodes only. In the bulk plasma, stepwise ionization from the 1s$_5$ state is an important channel for ionization, as shown earlier, however, this process represents only a moderate loss in the balance of the 1s$_5$ metastable atoms. The axial diffusion of the metastable atoms, on the other hand, represents a major loss channel as well at the positions where the density of these atoms is high (see the curve 'AD−' in panel (d) of figure 11). This process results in a flux of Ar 1s$_5$ atoms both towards the electrodes and towards the center of the discharge. In this latter domain,

therefore, the axial diffusion creates a source for these species, as indicated by the curve 'AD+'.

The density of the Ar atoms in the 1s$_5$ state exceeds significantly the ion density in the plasma, as shown in figure 12(a) for the discharge center. The ratio is the largest at the medium pressure of 15 Pa, in this case the density of metastable atoms is more than an order magnitude higher than the ion density. The high density of metastables results as well in high fluxes of these atoms at the electrode surfaces. The data shown in figure 12(b) reveal that the Ar 1s$_5$ flux increases with increasing pressure. Recall that with increasing pressure the peak of the production rate of these atoms approaches the electrodes due to the decreasing sheath width, therefore the decreasing trend of the Ar 1s$_5$ density with increasing p in the center of the plasma does not contradict the increasing metastable flux at the electrodes. The ion flux is generally a factor of few higher compared to the Ar 1s$_5$ flux, for the parameters covered here.

While secondary electron production at the electrodes is not expected to contribute in a major way to the maintenance of the plasma at the conditions studied, at higher RF voltages and/or pressures secondary electrons may have a significant contribution. Under such conditions the present approach may help quantifying the contributions of positive ions and metastables to secondary electron production [61].
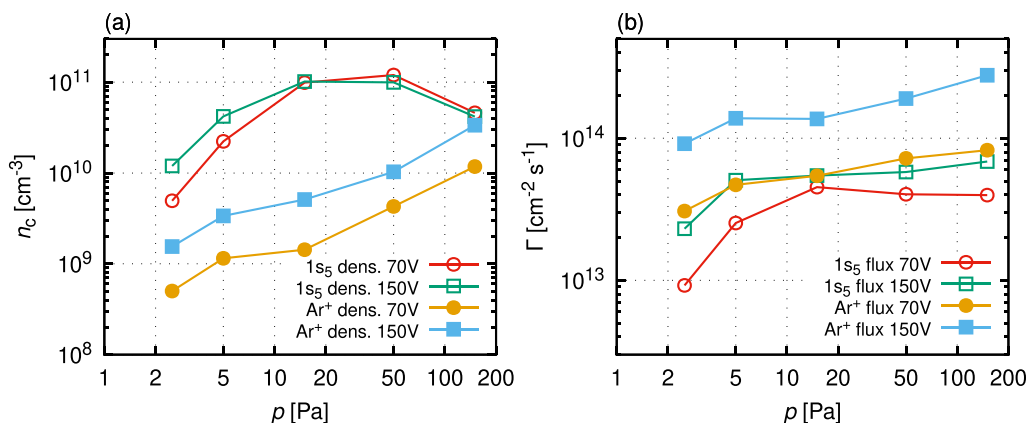
Figure 12. Densities of Ar atoms in $1s_5$ state and Ar^+ ions in the center of the plasma as a function of pressure (a) and the fluxes of these species at the electrodes (b).

5. Summary

We have investigated the kinetics of excited atoms in a low-pressure argon CCP source using numerical simulations and experiments. The simulations have been based on an extended particle-in-cell/Monte Carlo collisions (PIC/MCC) code coupled with a diffusion-reaction-radiation (DRR) code. The PIC/MCC code considered as 'targets' for electron-impact collisions Ar atoms in 30 excited states besides the GS atoms. The spatial distributions of the Ar atoms in these excited states were computed by the DRR code, considering the electron-impact source and loss rates of these atoms computed in the PIC/MCC code as well as additional processes, including diffusive transport of the atoms in the excited states, pooling ionization reactions, the quenching of the metastable states by neutral atoms, as well as radiation processes. The simulations were executed with gas temperature values measured experimentally, using the TDLAS method which also yielded the spatial density profiles of the Ar $1s_5$ atoms.

At the lowest pressure of 2.5 Pa, atoms in excited states were found not to influence the ion production in the plasma significantly. With an increasing pressure, however, the density of the atoms in the excited states increased remarkably and this resulted in the emergence of significant ion production via the stepwise and pooling ionization processes. The presence of these reactions resulted in an appreciable (factor of few) enhancement of the plasma density. Under these conditions the spatial profile of the plasma density changed as well, as the reactions mentioned above are also 'active' in the central region of the discharge, unlike the electron impact ionization process that concentrates mainly near the sheath edge regions. The presence of the excited states influences as well the energy distribution of the electrons. As many of the stepwise excitation processes have threshold energies in the $\sim$eV range, the EEPF becomes depleted above this energy.

The simulations made it possible to determine the spatial distributions of Ar atoms in all the excited states considered and all the source and loss rates of the excited states. Among these, only the rates influencing the $1s_5$ state were discussed in details. At low pressure this state was found to be created

primarily by electron impact excitation of the GS Ar atoms and by radiation from the atoms in the 2p states. Stepwise excitation and diffusion losses were identified as major loss channels for this state at the same conditions. At higher pressures, the dominant loss processes become the stepwise excitation processes to other 1s and 2p states.

The comparison of the computed and measured spatial density profiles of the Ar $1s_5$ atoms showed a good agreement, with some differences in the absolute values of the density. The higher density values obtained in the calculations as compared to the experimental values can be explained by the fact that the simulation is spatially one-dimensional (although it considers the radial diffusion loss of the atoms in the excited states), while in the experiments the metastable density is derived from the absorption of the laser light along a line over the diameter of the plasma confined in a cylindrical chamber. As other possible sources of errors the limited accuracy of the input data and the negligence of high-lying excited states can be mentioned. Related to the latter, in [47] it was pointed out that higher excited states can influence the populations of the 1s and 2p states via cascades to a considerable extent. As future work, we consider both adding more elementary processes related to these higher excited states for improving accuracy and also identifying less important reactions in the present model in order to build a more efficient simulation code.

Data availability statement

The data that support the findings of this study are available upon reasonable request from the authors.

Acknowledgments

ORCID iDs

Zoltán Donkó ⓘ https://orcid.org/0000-0003-1369-6150
Peter Hartmann ⓘ https://orcid.org/0000-0003-3572-1310
Ihor Korolov ⓘ https://orcid.org/0000-0003-2384-1243
David Schulenberg ⓘ https://orcid.org/0000-0002-4086-8678
Shahid Rauf ⓘ https://orcid.org/0000-0001-5689-6115
Julian Schulze ⓘ https://orcid.org/0000-0001-7929-5734

References

[1] Makabe T and Petrović Z 2006 *Plasma Electronics: Applications in Microelectronic Device Fabrication* (London: Taylor & Francis)

[2] Chabert P and Braithwaite N 2011 *Physics of Radio-Frequency Plasmas* (New York: Cambridge University Press)

[3] Lieberman M A and Lichtenberg A J 2005 *Principles of Plasma Discharges and Materials Processing* 2nd edn (Hoboken, NJ: Wiley)

[4] Graves D B 1994 *IEEE Trans. Plasma Sci.* **22** 31–42

[5] Kambara M, Kawaguchi S, Lee H J, Ikuse K, Hamaguchi S, Ohmori T and Ishikawa K 2022 *Jpn. J. Appl. Phys.* **62** SA0803

[6] Chabert P, Tsankov T V and Czarnetzki U 2021 *Plasma Sources Sci. Technol.* **30** 024001

[7] Zhang Y-R, Bogaerts A and Wang Y-N 2012 *J. Phys. D: Appl. Phys.* **45** 485204

[8] Becker M M, Kählert H, Sun A, Bonitz M and Loffhagen D 2017 *Plasma Sources Sci. Technol.* **26** 044001

[9] Verboncoeur J P 2005 *Plasma Phys. Control. Fusion* **47** A231–60

[10] Donkó Z 2011 *Plasma Sources Sci. Technol.* **20** 024001

[11] Kushner M J 2009 *J. Phys. D: Appl. Phys.* **42** 194013

[12] Economou D J 2017 *Plasma Process. Polym.* **14** 1600152

[13] Birdsall C K 1991 *IEEE Trans. Plasma Sci.* **19** 65–85

[14] Tskhakaya D, Matyash K, Schneider R and Taccogna F 2007 *Contrib. Plasma Phys.* **47** 563–94

[15] Turner M M 2006 *Phys. Plasmas* **13** 033506

[16] Matyash K, Schneider R, Taccogna F, Hatayama A, Longo S, Capitelli M, Tskhakaya D and Bronold F 2007 *Contrib. Plasma Phys.* **47** 595–634

[17] Denpoh K and Nanbu K 1998 *J. Vac. Sci. Technol.* A **16** 1201–6

[18] Denpoh K D K and Nanbu K N K 2000 *Jpn. J. Appl. Phys.* **39** 2804

[19] Gudmundsson J T, Kawamura E and Lieberman M A 2013 *Plasma Sources Sci. Technol.* **22** 035011

[20] Sun A, Becker M M and Loffhagen D 2016 *Comput. Phys. Commun.* **206** 35–44

[21] Lafleur T, Chabert P, Turner M and Booth J P 2013 *Phys. Plasmas* **20** 124503

[22] Donkó Z, Derzsi A, Vass M, Horváth B, Wilczek S, Hartmann B and Hartmann P 2021 *Plasma Sources Sci. Technol.* **30** 095017

[23] Korolov I, Donko Z, Hübner G, Bischoff L, Hartmann P, Gans T, Liu Y, Mussenbrock T and Schulze J 2019 *Plasma Sources Sci. Technol.* **28** 094001

[24] Gudmundsson J, Kouznetsov I, Patel K and Lieberman M 2001 *J. Phys. D: Appl. Phys.* **34** 1100

[25] Gudmundsson J 2004 *J. Phys. D: Appl. Phys.* **37** 2073

[26] Segawa S S S, Kurihara M K M, Nakano N N N and Makabe T M T 1999 *Jpn. J. Appl. Phys.* **38** 4416

[27] Song S-H and Kushner M J 2012 *Plasma Sources Sci. Technol.* **21** 055028

[28] Brandt S, Berger B, Donkó Z, Derzsi A, Schüngel E, Koepke M and Schulze J 2019 *Plasma Sources Sci. Technol.* **28** 095021

[29] Denpoh K and Nanbu K 2022 *J. Vac. Sci. Technol.* A **40** 063007

[30] Makabe T 2022 *J. Phys. D: Appl. Phys.* **56** 045203

[31] Vass M, Wilczek S, Derzsi A, Horváth B, Hartmann P and Donkó Z 2022 *Plasma Sources Sci. Technol.* **31** 045017

[32] Roberto M, Smith H B and Verboncoeur J P 2003 *IEEE Trans. Plasma Sci.* **31** 1292–8

[33] Wen D-Q, Krek J, Gudmundsson J T, Kawamura E, Lieberman M A and Verboncoeur J P 2021 *Plasma Sources Sci. Technol.* **30** 105009

[34] Siepa S L 2017 Global collisional-radiative model for optical emission spectroscopy of argon and argon-containing plasmas *PhD Thesis Dissertation*, Ruhr-Universität Bochum, Bochum

[35] Ferreira C, Loureiro J and Ricard A 1985 *J. Appl. Phys.* **57** 82–90

[36] Stankov M, Becker M M, Hoder T and Loffhagen D 2022 *Plasma Sources Sci. Technol.* **31** 125002

[37] Lauro-Taroni L, Turner M and Braithwaite N S 2004 *J. Phys. D: Appl. Phys.* **37** 2216

[38] Zheng B, Fu Y, Wen D-Q, Wang K, Schuelke T and Fan Q H 2020 *J. Phys. D: Appl. Phys.* **53** 435201

[39] Wen D-Q, Krek J, Gudmundsson J T, Kawamura E, Lieberman M A and Verboncoeur J P 2022 *IEEE Trans. Plasma Sci.* **50** 2548–57

[40] McMillin B K and Zachariah M R 1995 *J. Appl. Phys.* **77** 5538–44

[41] Boffard J B, Piech G A, Gehrke M F, Anderson L and Lin C C 1999 *Phys. Rev.* A **59** 2749

[42] Piech G A, Boffard J B, Gehrke M F, Anderson L and Lin C C 1998 *Phys. Rev. Lett.* **81** 309

[43] Sharma L, Srivastava R and Stauffer A 2007 *Phys. Rev.* A **76** 024701

[44] Gangwar R, Sharma L, Srivastava R and Stauffer A 2012 *J. Appl. Phys.* **111** 053307

[45] Zatsarinny O 2006 *Comput. Phys. Commun.* **174** 273–356

[46] Zatsarinny O and Bartschat K 2013 *J. Phys. B: At. Mol. Opt. Phys.* **46** 112001

[47] Bogaerts A, Gijbels R and Vlcek J 1998 *J. Appl. Phys.* **84** 121–36

[48] Kano K, Suzuki M and Akatsuka H 2000 *Plasma Sources Sci. Technol.* **9** 314

[49] Schulze M, Yanguas-Gil A, Von Keudell A and Awakowicz P 2008 *J. Phys. D: Appl. Phys.* **41** 065206

[50] Akatsuka H 2019 *Adv. Phys.* X **4** 1592707

[51] Zhu X-M and Pu Y-K 2009 *J. Phys. D: Appl. Phys.* **43** 015204

[52] Horita H, Kuwahara D, Akatsuka H and Shinohara S 2021 *AIP Adv.* **11** 075226

[53] Zhu X M, Pu Y K, Celik Y, Siepa S, Schüngel E, Luggenhölscher D and Czarnetzki U 2012 *Plasma Sources Sci. Technol.* **21** 024003

[54] Boffard J B, Jung R, Lin C C and Wendt A 2009 *Plasma Sources Sci. Technol.* **18** 035017

[55] Kovalev A, Kurchikov K, Proshina O, Rakhimova T, Vasilieva A and Voloshin D 2019 *Phys. Plasmas* **26** 123501

[56] Chai K-B and Kwon D-H 2019 *J. Quant. Spectrosc. Radiat. Transfer* **227** 136–44

[57] Kovalev A, Rakhimova T, Rakhimov A, Proshina O, Vasilieva A and Voloshin D 2021 *Phys. Plasmas* **28** 093507

[58] Gans T, Schulz-Von Der Gathen V and Döbele H 2004 *Europhys. Lett.* **66** 232

[59] Ellingboe A, Boswell R, Booth J and Sadeghi N 1995 *Phys. Plasmas* **2** 1807–9

[60] Schulze J, Gans T, O'Connell D, Czarnetzki U, Ellingboe A and Turner M 2007 *J. Phys. D: Appl. Phys.* **40** 7008
[61] Phelps A and Petrovic Z L 1999 *Plasma Sources Sci. Technol.* **8** R21
[62] Bogdanova M, Lopaev D, Zotovich A, Proshina O, Rakhimova T, Zyryanov S and Rakhimov A 2022 *Plasma Sources Sci. Technol.* **31** 094001
[63] Marić D, Savić M, Sivoš J, Škoro N, Radmilović-Radjenović M, Malović G and Petrović Z L 2014 *Eur. Phys. J D* **68** 1–7
[64] Bokhan P, Gugin P, Lavrukhin M, Kim V, Shevchenko G and Zakrevsky D 2022 *Plasma Sources Sci. Technol.* **31** 125009
[65] Gudmundsson J T, Krek J, Wen D-Q, Kawamura E and Lieberman M 2022 *Plasma Sources Sci. Technol.* **30** 125011
[66] Bsr database (available at: www.lxcat.net/BSR) (Accessed 18 August 2022)
[67] Pitchford L C *et al* 2017 *Plasma Process. Polym.* **14** 1600098
[68] Carbone E, Graef W, Hagelaar G, Boer D, Hopkins M M, Stephens J C, Yee B T, Pancheshnyi S, van Dijk J and Pitchford L 2021 *Atoms* **9** 16
[69] Phelps A V 1994 *J. Appl. Phys.* **76** 747–53
[70] Kim H, Iza F, Yang S, Radmilović-Radjenović M and Lee J 2005 *J. Phys. D: Appl. Phys.* **38** R283
[71] Lymberopoulos D P and Economou D J 1995 *J. Res. Natl Inst. Stand. Technol.* **100** 473
[72] Schulenberg D A, Korolov I, Donkó Z, Derzsi A and Schulze J 2021 *Plasma Sources Sci. Technol.* **30** 105003
[73] Schulze C, Donkó Z and Benedikt J 2022 *Plasma Sources Sci. Technol.* **31** 105017
[74] Hyman H 1979 *Phys. Rev. A* **20** 855
[75] Lymberopoulos D P and Economou D J 1993 *J. Appl. Phys.* **73** 3668–79
[76] Ellis E and Twiddy N 1969 *J. Phys. B: At. Mol. Phys.* **2** 1366

[77] Tachibana K 1986 *Phys. Rev.* A **34** 1007
[78] Turner M M, Derzsi A, Donko Z, Eremin D, Kelly S J, Lafleur T and Mussenbrock T 2013 *Phys. Plasmas* **20** 013507
[79] Zatsarinny O, Wang Y and Bartschat K 2014 *Phys. Rev. A* **89** 022706
[80] Capriotti E R 1965 *Astrophys. J.* **142** 1101
[81] Bhatia A and Kastner S 2000 *J. Quant. Spectrosc. Radiat. Transfer* **67** 55–63
[82] Stefanović I, Kuschel T, Schröter S and Böke M 2014 *J. Appl. Phys.* **116** 113302
[83] Bánó G and Donkó Z 2012 *Plasma Sources Sci. Technol.* **21** 035011
[84] Hübner S, Sadeghi N, Carbone E A D and van der Mullen J J A M 2013 *J. Appl. Phys.* **113** 143306
[85] Sadeghi N, Magnan R and Massines F 2022 *J. Quant. Spectrosc. Radiat. Transfer* **288** 108264
[86] Liu W-Y, Xu Y, Liu Y-X, Peng F, Guo Q, Li X-S, Zhu A-M and Wang Y-N 2015 *J. Appl. Phys.* **117** 023306
[87] SADEGHI N 2004 *J. Plasma Fusion Res.* **80** 767–76
[88] Kramida A, Ralchenko Y and Reader J (NIST ASD Team) 2022 *NIST Atomic Spectra Database* (ver. 5.10)(Gaithersburg, MD: National Institute of Standards and Technology)(https://physics.nist.gov/asd) (Accessed 23 February 2023)
[89] Derzsi A, Hartmann P, Vass M, Horváth B, Gyulai M, Korolov I, Schulze J and Donkó Z 2022 *Plasma Sources Sci. Technol.* **31** 085009
[90] Schulze J, Donko Z, Derzsi A, Korolov I and Schuengel E 2014 *Plasma Sources Sci. Technol.* **24** 015019
[91] Carbone E, van Veldhuizen E, Kroesen G and Sadeghi N 2015 *J. Phys. D: Appl. Phys.* **48** 425201
[92] Yamasaki M, Yagisawa T and Makabe T 2014 *Jpn. J. Appl. Phys.* **53** 036001